

# UC San Diego

## UC San Diego Previously Published Works

### Title

Temperature Dependent Spin Dynamics in La<sub>0.67</sub>Sr<sub>0.33</sub>MnO<sub>3</sub>/Pt Bilayers

### Permalink

<https://escholarship.org/uc/item/5pb2n1tf>

### Authors

Sahoo, Biswajit

K, Akilan

Matthews, Katherine

et al.

### Publication Date

2025

### DOI

10.1002/admi.202401038

### Supplemental Material

<https://escholarship.org/uc/item/5pb2n1tf#supplemental>

### Copyright Information

This work is made available under the terms of a Creative Commons Attribution License, available at <https://creativecommons.org/licenses/by/4.0/>

Peer reviewed

# Temperature dependent spin dynamics in $\text{La}_{0.67}\text{Sr}_{0.33}\text{MnO}_3/\text{Pt}$ bilayers.

**Biswajit Sahoo\***, Akilan K, Katherine Matthews, Alexandre Pofelski, Alex Frano, Eric E Fullerton, Sebastien Petit-Watelot, Juan-Carlos Rojas Sanchez\* and Sarmistha Das\*

**\*Corresponding authors**

B. Sahoo, Eric E Fullerton

Center for Memory and Recording Research, University of California, San Diego, CA 92093, USA

Email: [bsahoo@ucsd.edu](mailto:bsahoo@ucsd.edu);

B. Sahoo, K. Matthews, A. Frano, S. Das

Department of Physics, University of California, San Diego, CA 92093, USA

Email: [sdas@physics.ucsd.edu](mailto:sdas@physics.ucsd.edu);

A. Pofelski:

Brookhaven National Laboratory, 98 Rochester St, Upton, NY 11973, USA

Email: [apofelski@bnl.gov](mailto:apofelski@bnl.gov)

Akilan K., S. Petit-Watelot, J-C. R. Sanchez

Institut Jean Lamour Université Lorraine - CNRS (UMR 7198) Campus Artem, F-54011 Nancy Cedex, France

Email: [juan-carlos.rojas-sanchez@univ-lorraine.fr](mailto:juan-carlos.rojas-sanchez@univ-lorraine.fr)

*Complex ferromagnetic oxides such as  $\text{La}_{0.67}\text{Sr}_{0.33}\text{MnO}_3$  (LSMO) offer pathways for creating energy-efficient spintronic devices with new functionalities. LSMO exhibits high-temperature ferromagnetism, half metallicity, sharp resonance linewidth, low damping and a large anisotropic magnetoresistance response. Combined with Pt, a proven material with high spin-charge conversion efficiency, LSMO can be used to create robust nano-oscillators for neuromorphic computing. Ferromagnetic resonance (FMR) and device level spin-pumping FMR measurements are performed to investigate the magnetization dynamics and spin transport in  $\text{NdGaO}_3(110)/\text{LSMO}(15\text{ nm})/\text{Pt}(0\text{ and }5\text{ nm})$  thin films ranging from 300K to 90K and compare the device performance with  $\text{Py}(7\text{ nm})/\text{Pt}(5\text{ nm})$  sample. The spin current pumped into Pt is quantified to determine the temperature dependent influence of interfacial interactions. The generated spin current in the micro-device is maximum at 170K for the optimally grown LSMO/Pt films. Additionally, this bilayer system exhibits low magnetic Gilbert damping (0.002), small linewidth (12 Oe) and a large spin Hall angle ( $\approx 3.2\%$ ) at 170K. Ex-situ deposited LSMO/Pt bilayers demonstrate excellent dynamic response, exhibiting fourfold enhancement in signal output, eightfold reduction in damping, and a threefold reduction in linewidth as compared to the Pt/Py system. Such robust device level performance can pave way for energy-efficient spintronic based devices.*

**Keywords:** Ferromagnetic resonance, spin pumping, spintronic devices, complex perovskite thin films, micro-devices.

Spin-based oscillators have potential for various communication applications such as radio frequency (RF) signal generator, modulator and detectors(1, 2) and can enable the development of low-power neuromorphic computing systems(3). There are two basic classes of spin-based oscillators: spin-transfer-torque (STT) oscillators and spin-orbit-torque (SOT) oscillators(4) which differ on the mechanism of conversion of charge to spin currents. Common requisites for the development of energy efficient oscillators are high charge-to-spin current conversion, low Gilbert damping of the ferromagnetic (FM) or ferrimagnetic layer and a sharp ferromagnetic resonance (FMR) linewidth. A smaller damping and FMR linewidth lower the critical current required for auto-oscillation, along with generation of a large output signal from the oscillator. Currently, the most commonly used materials for SOT oscillators systems are all metallic bilayers made of ferromagnet (FM)/ heavy metal (HM) (FM=CoFeB, NiFe, *etc.* ; HM=Pt, Ta, W, *etc.*...)(5, 6) where the spin-orbit interactions in HM layer generates spin currents via the spin Hall effect. For FM metals, the Gilbert damping is of the order of  $10^{-2}$  and FMR linewidths are of the order of 50 Oe or more(7–12).

To enhance nano-oscillator performance, transitioning towards complex oxides has the promise for improved functionality. Half-metallic perovskite FM  $\text{La}_{0.67}\text{Sr}_{0.33}\text{MnO}_3$  (LSMO) is a candidate material as the FM layer for SOT oscillators. LSMO has a very low damping(13), nearly 100% spin polarization(14), and exhibits a colossal magnetoresistance(15). Here we report our studies of LSMO/Pt bilayers where Pt is metallic with a large charge to spin conversion efficiency. There have been reports of FMR and inverse spin Hall effect (ISHE) experiments on LSMO/Pt heterostructures showing a low damping and a reasonable charge to spin conversion(16–21). These experiments were conducted on unpatterned LSMO films with relatively thick layers ( $t_{\text{LSMO}} > 20$  nm), primarily at room temperature (RT), which is near the Curie temperature ( $T_C$ ) of LSMO. The key finding from these studies is that LSMO/Pt structures exhibit a low damping factor, approximately 0.007–0.01, and a spin Hall angle in the range of 1.2–2.2%(16, 19). Some work on the temperature dependence of spin currents on LSMO/Pt has been reported, where an increase in spin current transmission with reduced temperature was observed (21). However, these measurements were done in LSMO(45 nm)/Pt(10 nm) on unpatterned samples of 5 x 1 x 0.5 mm, which can downplay the contribution of interfacial effects. To date, the temperature dependence of spin-charge conversion in LSMO/Pt thin films below 300 K with  $t_{\text{LSMO}} < 20$  nm, as detected by spin pumping voltage at the device level, remains unexplored.

For many spintronic and neuromorphic applications, one requires robust nano/micron size devices formed from low thickness of the FM and HM layer to enhance interfacial effects(22). The properties of thin film system may be altered after the harsh conditions of device fabrication such as exposure to high vacuum environments for contact deposition, high energy ion bombardment for etching and sonication in chemicals and solvents. For perovskites, such environments can cause generation of defects by various pathways such as sample damage(23), oxygen concentration change(24) *etc.*, which may give sub-optimal device-based performance, despite showing robust properties in unpatterned films.

The increased magnetization and lower damping(25, 26) of LSMO thin films at lower temperatures can potentially pump larger spin currents into the adjacent HM, enabling larger output voltage signals and energy efficient device performance. Thus, it is worthwhile investigating the temperature dependent magnetization dynamics of LSMO/ Pt system and the role of the interface for spin transport, both at the thin film and the device level. The inclusion of Pt will lower the device resistance enabling robust device stability and optimal response to currents. The samples considered here are LSMO(15 nm) films and LSMO(15 nm)/Pt(5 nm) bilayers grown on  $\text{NdGaO}_3$ (110)(NGO(110)) single-crystal substrates. NGO(110)

substrates were used as they do not have the high relative permittivity and dielectric loss of some commonly used oxide substrates, such as  $\text{SrTiO}_3$ , which can otherwise cause significant current shunting in substrates at high frequency even at RT, and may strongly affect spin-torque measurement resulting in an inaccurate estimation of charge-to-spin conversion efficiency(27).

We perform temperature dependent FMR on unpatterned films where we detect the absorbed microwave power, and spin-pumping FMR (SP-FMR) on patterned microdevices where we detect the spin pumping voltage. We quantify the evolution of the linewidth, effective magnetization, intrinsic Gilbert damping, spin current density and the spin Hall angle (SHA) versus temperature to find the best conditions to create an energy efficient spin Hall nano-oscillator and related devices. We further provide comparison between LSMO/Pt and the conventionally used Py/Pt devices fabricated under same conditions to show the efficacy of the LSMO/Pt system in device-based applications. Our results also provide concrete insights on the role played by the interfacial layer for spin transport across the LSMO/Pt interface.

Epitaxial LSMO films were grown using pulsed laser deposition on NGO(110) substrates. Figure 1 shows the transmission electron microscopy (TEM) image of the NGO/LSMO sample displaying a highly epitaxial cube-on-cube growth of LSMO on NGO. LSMO grows in the 001 direction as demonstrated by the X-ray diffraction spectra (Fig. S1(a)) and the electron diffraction (Fig. 1(b)).

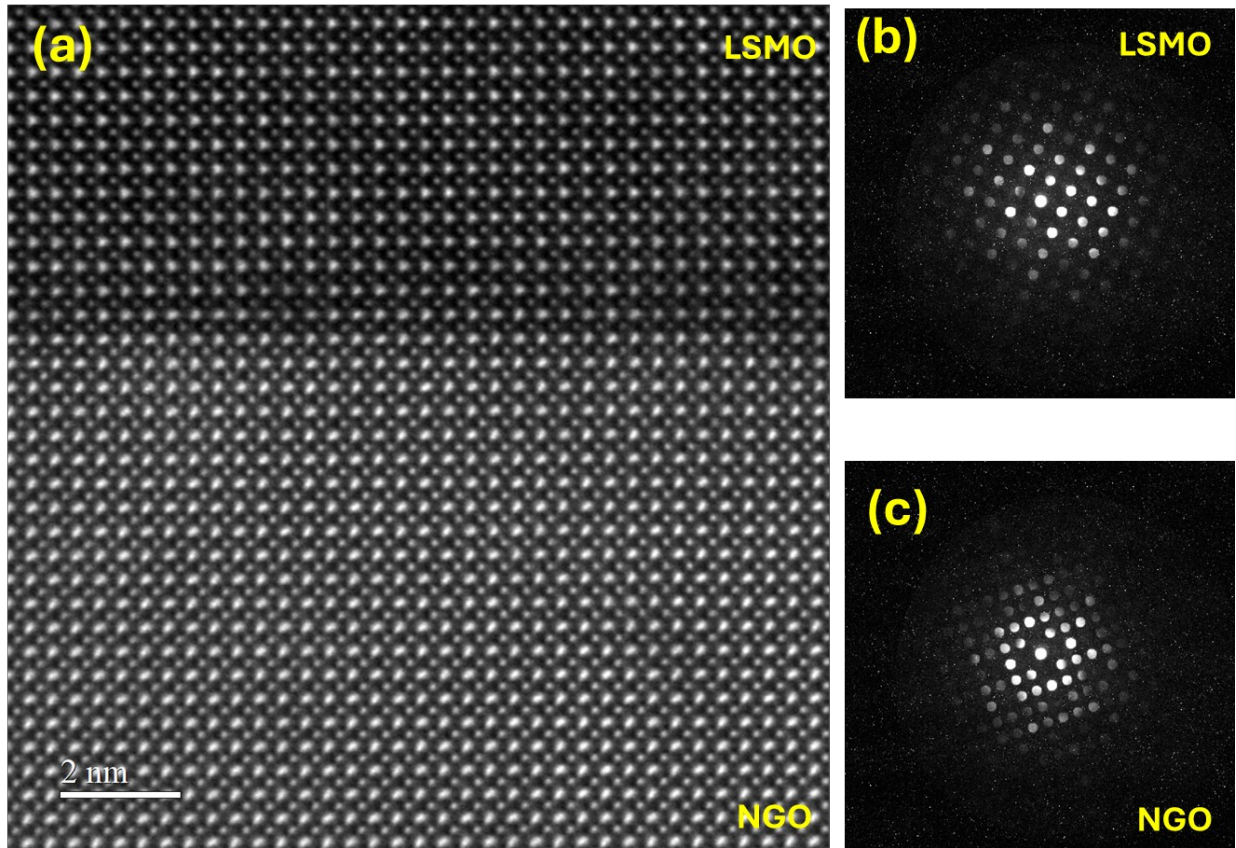


Figure 1 TEM image of NGO(110)/LSMO(15) showing epitaxial growth. (b) and (c) show the electron diffraction pattern for LSMO and NGO respectively establishing a highly crystalline structure.

The sample was transported quickly through the air into a sputtering chamber where Pt was deposited. The sample fabrication details are provided in the supplementary.

The resistance-vs.-temperature measurements (Figs. S4(a)) for LSMO show a typical semi-metallic behavior, with resistivity values  $3\text{m}\Omega\text{-cm}$  at RT similar to those reported in the literature(28). For LSMO/Pt (Fig. S4(b)), the resistivity is  $28\mu\Omega\text{-cm}$  at RT, is similar to that measured for Pt thin films(11, 29), indicating that the majority of the current shunts through the Pt layer.

The FMR measurements were performed using a field-modulated, flip-chip co-planar waveguide, in conjunction with a cryogenic set-up. FMR measurements were performed at a frequency range of 5-15 GHz at 1 GHz intervals at temperatures ranging from 300K to 90K. Various magnetic parameters were obtained at all temperatures from analysis of the FMR spectra. Figure 2 shows the FMR spectra of LSMO and LSMO/Pt at 5GHz for different temperatures. At 300K, the signal consists of two modes which merge into a single mode at lower temperatures ( $T \leq 250\text{K}$ ). This may be due to the presence of multiple collective oscillation modes as a result of weaker exchange interaction of LSMO at RT, which increases at lower temperatures(30) enabling the emergence of a single sharp peak. Increase in the saturation magnetization ( $M_s$ ) shifts the resonance field to lower values with reducing temperature. A similar trend is observed in the LSMO/Pt sample. For fitting of a single FMR mode, we use the sum of symmetric and anti-symmetric Lorentzian function:

$$\frac{dP}{dH} = \text{off} + mH + S_1 \frac{\Delta H^2 - 4(H - H_{res})^2}{(4(H - H_{res})^2 + \Delta H^2)^2} - 4A_1 \frac{\Delta H(H - H_{res})}{(4(H - H_{res})^2 + \Delta H^2)^2} \quad (1)$$

where  $H_{res}$  is the resonant field,  $\Delta H$  is the full width at half maximum;  $m$  and  $\text{off}$  are the slope and offset, respectively. For the 300-K spectra, which has two peaks, we employ a two-mode fitting approach using two pairs of symmetric and anti-symmetric Lorentzian functions. The results of the fits are shown in Figs. 2 and S5.

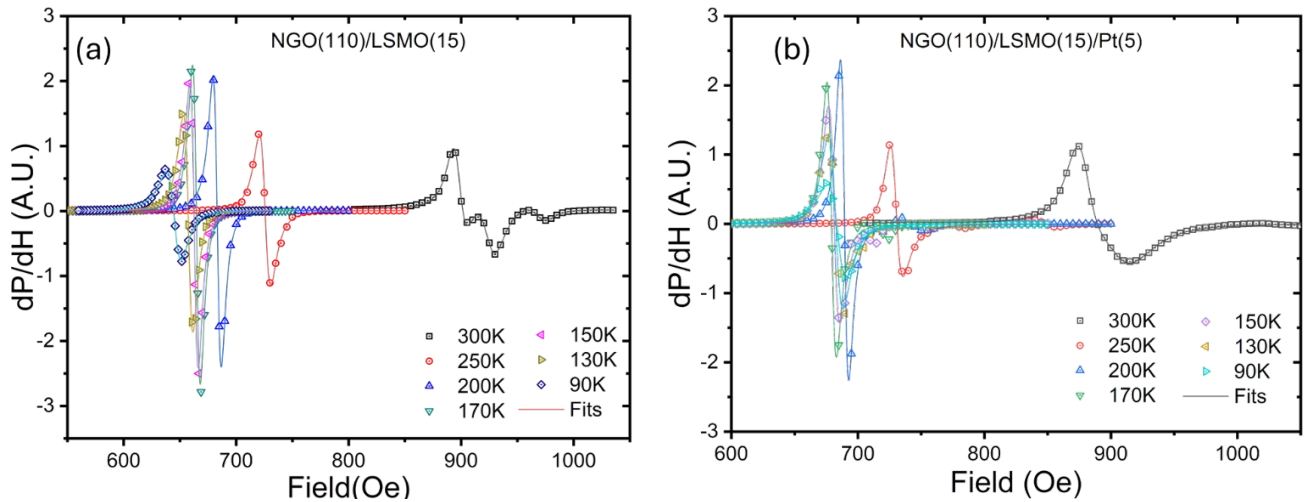


Figure 2 (a) and (b) show the temperature dependent FMR spectra measured at 5 GHz for LSMO and LSMO/Pt, respectively. Solid lines are the fits to the data. The lineshape for both the samples shows a similar variation with multiple peaks at 300K, which combine into a single mode at lower temperatures.

We fit the  $H_{res}$  vs. frequency data to the Kittel equation(31):

$$f = \frac{\gamma}{2\pi} \sqrt{(H_k + H_{res})(H_k + H_{res} + 4\pi M_{eff})}$$

(2)

where  $\gamma$  is the gyromagnetic ratio,  $H_k$  is the in-plane uniaxial anisotropy field and  $M_{eff}$  is the effective magnetization.

We now focus on the behavior of the resonant fields of the two samples with temperature. We find that from 300K up until 170K, the  $H_{res}$  values are approximately the same indicating the Pt layer is not significantly affecting the magnetic environment of the underlying LSMO. However, below 170K, the  $H_{res}$  of LSMO shows a lower value as opposed to LSMO/Pt (Fig. S7(b)). A similar trend is observed in the  $M_s$  vs T measurements (Fig. S8(b)) wherein we see a reduction in the  $M_s$  for LSMO/Pt below 150K with an approximately 12% reduction at 90K.

The  $M_{eff}$  obtained from FMR is lower with respect to the  $M_s$  obtained from VSM experiments (Fig. S8(b)). The lower  $M_{eff}$  value indicates an additional perpendicular magnetic anisotropy (PMA) as  $M_{eff} = M_s - H_a/4\pi$ , where  $H_a$  is the out-of-plane (OOP) anisotropy field that is present in both the LSMO and LSMO/Pt films. This is confirmed by OOP magnetometry of LSMO, where we observe increasing contribution of  $H_a$  with reduced temperatures (Fig. S8(d)) as the OOP saturation field is much lower than  $4\pi M_s$ . Such PMA has been attributed to magnetostriction due to interfacial strain(26, 27). A similar trend is observed in the  $M_{eff}$  vs T measurement as well, wherein we see a lower value of  $M_{eff}$  from T<150K for LSMO/Pt. These observations suggest that addition of Pt layer at the top may have led to a formation of a thin interfacial region at the top interface, which shows similar magnetic properties as bulk LSMO between 170K<T<300K but shows a reduced  $M_s$  below 150K. As the value of  $M_s$  is lower for LSMO/Pt, magnetic proximity effects such as magnetic moment induction in Pt (32, 33), which generally enhances the magnetic moment(34), may not be present in LSMO/Pt bilayers. Additionally, the ex-situ deposition of Pt, may not provide the best conditions for observation of such interface sensitive effects.

To obtain the intrinsic damping, we fit the line-width vs frequency to the following equation:

$$\Delta H = \Delta H_0 + \frac{4\pi\alpha}{\gamma} f$$

(3)

where  $\Delta H_0$  is the inhomogeneous linewidth broadening,  $\alpha$  is the intrinsic Gilbert damping, and  $\gamma$  is the gyromagnetic ratio obtained from Eq. (2). Figs. 3(a) and (b) show the fits to the  $f$  vs  $\Delta H$  curves using Eq. (3). It should be noted that there can be additional contributions to the linewidth broadening (2-magnon scattering, mosaicity broadening etc.), which can cause a non-linear variation of linewidth with frequency(35, 36). However, in our case, both LSMO and LSMO/Pt show a linear behavior of  $\Delta H$  with respect to frequency and thus these effects were not included in the analysis.

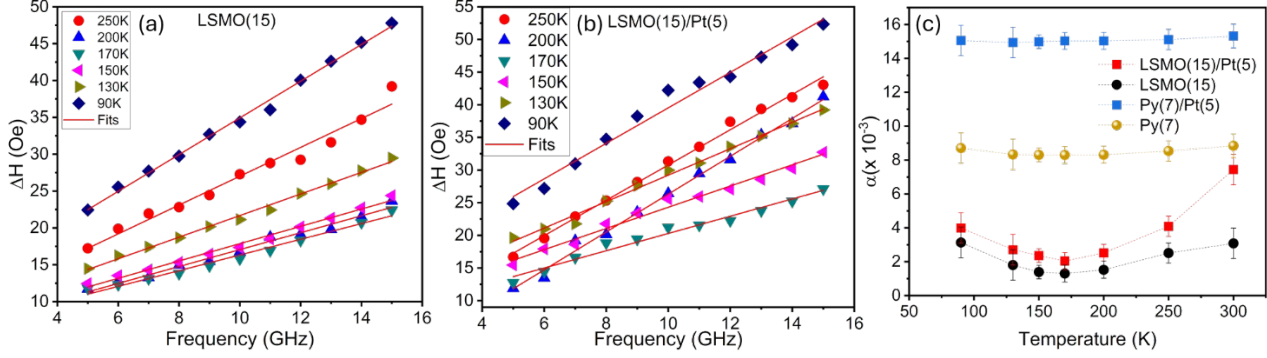


Figure 3 FMR results. (a) and (b) show the linewidth vs frequency plots for LSMO and LSMO/Pt, respectively (points) and the solid lines are fits to Eq. 3. The fits show a linear behavior indicating minimal contribution of two magnon scattering and other non-linear processes. (c) shows the variation of Gilbert damping with temperature of LSMO, LSMO/Pt, Py, and Py/Pt samples.

The variation of the Gilbert damping magnetic with respect to temperature for LSMO and LSMO/Pt is shown in Fig. 3(c). For LSMO, the damping is 0.003 at room temperature (RT), which is comparable to values reported in the literature for similar LSMO thickness values(19, 20, 25). The damping decreases with decreasing temperature, reaching a minimum value of 0.0013 at 170K and then increases to 0.0031 at 90K. Observation of such minima in the damping has also been reported in LSMO thin films(25, 26). LSMO/Pt follows a similar trend, albeit with an increased value of  $\alpha$  (0.007 at 300K, 0.002 at 170K and 0.004 at 90K), which can be attributed to additional spin pumping into the Pt layer<sup>7,20</sup>. In contrast, the damping for a reference Py(7) and Py(7)/Pt(5) bilayer over the same temperature range remains nearly constant at 0.008 and 0.015 respectively. Additionally, the inhomogeneous broadening is low in LSMO and LSMO/Pt indicating a high-quality magnetic layer growth in both samples (Fig. S6(b)).

The minima in damping with temperature can be explained by the Kambersky's torque correlation model(37) and its extensions(38, 39), which incorporate contribution of conductivity-like (based on the model of propagating spin waves in a breathing Fermi surface) and resistivity-like (based on spin flip due to magnon absorption) components into the intrinsic Gilbert damping. The increased damping at lower temperatures may also stem from the coupling between the magnetic moments of the metallic LSMO and a phase-separated magnetically active (PSMA) region, which is claimed to form at the top and bottom interfaces of LSMO and have anti-ferromagnetic moments(25, 40, 41). To gain further insight into the possible existence and nature of this region in our thin films, we performed EELS analysis of the Mn  $L_2$ - $L_3$  edge throughout the entire LSMO thickness at RT. Our results reveal an increase in the  $L_3/L_2$  ratio ( $L_{2,3}$ ) near both the bottom ( $L_{2,3}=2.45$ ) and the top interfaces ( $L_{2,3}=2.38$ ) as opposed to the bulk averaged value of 2.33 (Fig. 4(a)). The interfacial region has a thickness of  $< \approx 1.5$  nm for the top and  $< \approx 2.5$  nm for the bottom interface and is more pronounced at the bottom interface, presumably due to high temperature interaction of LSMO with NGO during sample growth, as opposed to RT deposition of Pt. In LSMO, the Mn ion exists as a mixed state of  $Mn^{+3}$  and  $Mn^{+4}$  state and the  $L_{2,3}$  indicates relative contribution of  $Mn^{+3}/Mn^{+4}$  state (41). The increase in  $L_{2,3}$  indicates a decrease in the Mn valency at the top and bottom interfaces. EELS spectra of the Mn  $L_{2,3}$  edge at 100K qualitatively does not show a significant change implying that the Mn valence state distribution remains largely unchanged at lower temperatures (Fig. 4(b)). However, increased noise due to significant sample drift at 100K limits the reliability of  $L_{2,3}$  calculations, as the values are highly sensitive to peak-fitting procedures.

Magnetometry measurements of LSMO and LSMO/Pt reveal no strong evidence of any significant AFM coupling due to absence of exchange bias, implying that this interaction may be very weak in our films due to the ultrathin (<1.5nm) interfacial layer. An increased coercivity is observed in LSMO/Pt, which may be a signature of AFM coupling, but this may also have contribution from the introduction of disorder in LSMO by Pt.(42, 43) . Enhanced magnetic interaction of different Mn oxidation states in the bulk and at the interfaces (e.g. double exchange interaction)(40, 44) at lower temperatures is proposed as an explanation for the observed increasing trend in damping for  $T < 150\text{K}$ . The diffusion of Nd into LSMO at the bottom interface, can lead to increased spin scattering in this layer (43) which may have more contribution than that at the top interface. This may explain the similar trend of damping enhancement at low temperatures, for both LSMO and LSMO/Pt.

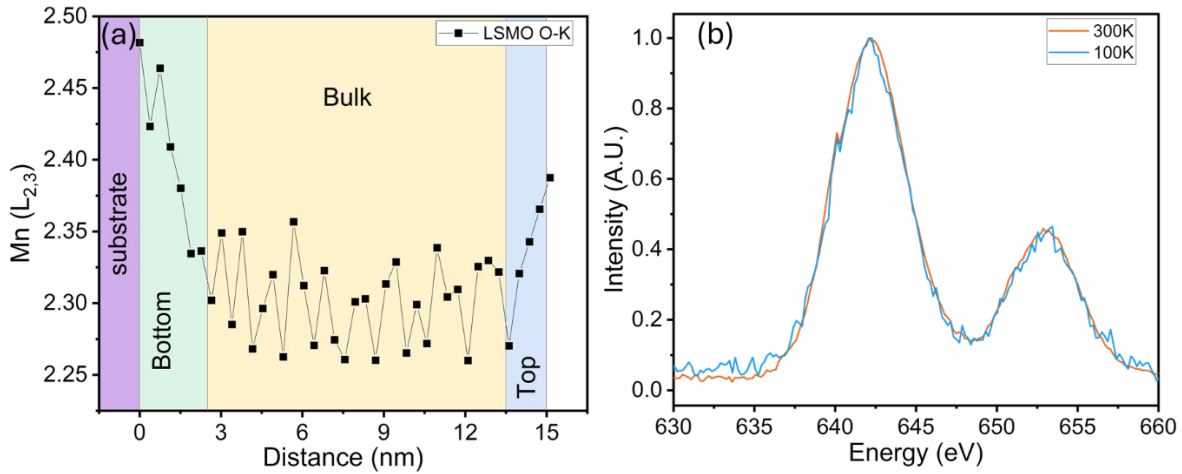


Figure 4 (a) shows the variation of Mn  $L_{2,3}$  across the LSMO thickness as obtained via EELS measurements at 300K, showing regions with a higher  $L_{2,3}$  (lower Mn valency) at the top and bottom interfaces. (b) shows the EELS spectra of Mn  $L_{2-3}$  edge of bulk LSMO at 300K and 100K indicating no significant difference.

Kambersky's model cannot account for the interactions arising from these layers which results in deviation from the damping fitting by this model (Fig. S6(a)). In the later sections, we provide direct evidence of the role of this layer in the transmission of spin current into Pt.

For quantifying the spin-to-charge conversion efficiency and the effects of the PSMA layer on spin transmission, the LSMO/Pt films were patterned into  $500 \times 10 \mu\text{m}$  devices via a 3 step optical lithography process for spin-pumping FMR (SP-FMR) measurements(45, 46). These measurements were performed from 5 to 15 GHz at 1 GHz intervals and 31.6 mW (15dBm) of input power, at the same temperatures as the FMR measurements. Figures 5(a)-(b) show the schematic of the set-up. An RF current is applied through ground-signal-ground (G-S-G) probes onto a waveguide patterned directly on the sample, which includes a  $50\text{-}\Omega$  terminator for impedance matching. Simultaneously, the external in-plane magnetic field applied is swept perpendicular to the direction of the radio frequency (RF) wave oscillation. The magnetic moments in the FM precess due to the resonance due to RF and DC field, and pure spin current is pumped into the adjacent HM. This spin current is converted into charge current by the inverse spin Hall effect in the HM layer, resulting in a measurable voltage that is detected by gold probes.

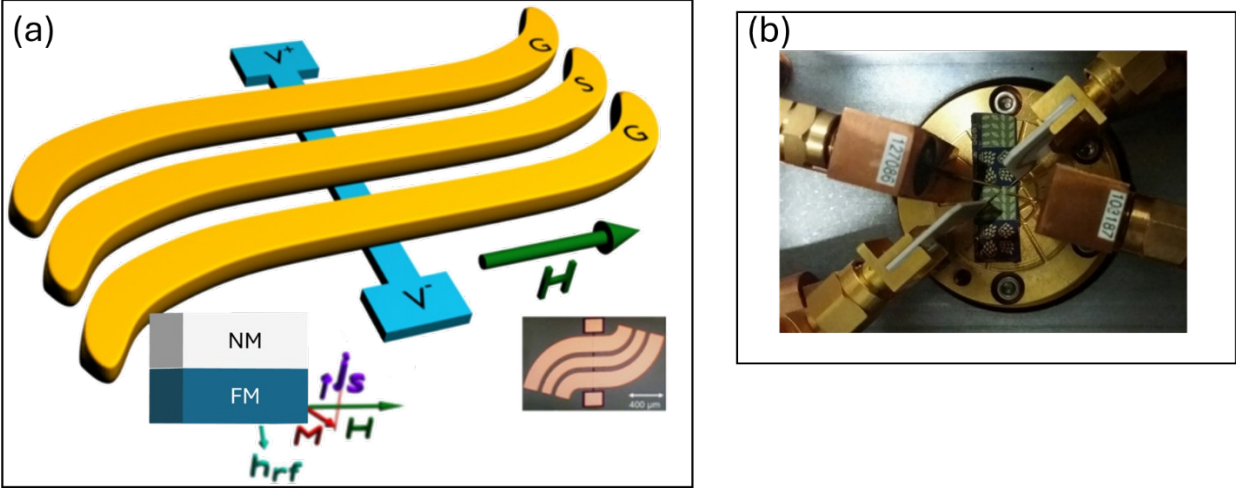


Figure 5 (a) shows the schematic of the SP-FMR measurement set-up. Inset bottom right shows a micrograph of the fabricated device. (b) shows the probe placement for measurement of the SP-FMR signals. The copper blocks (bottom right and top left) are the RF probe and the 50Ω terminator probe respectively. The top right and bottom left blocks are the voltage probes.

The resulting line-shape consists of symmetric and antisymmetric Lorentzian components, with a voltage maximum (or minimum) at the resonance field. The signals are fit to the following form:

$$V_{total} = V_s \frac{\left(\frac{\Delta H}{2}\right)^2}{\left(\frac{\Delta H}{2}\right)^2 + (H - H_{res})^2} + V_A \frac{\left(\frac{\Delta H}{2}\right)(H - H_{res})}{\left(\frac{\Delta H}{2}\right)^2 + (H - H_{res})^2}. \quad (4)$$

Here  $V_s$  is the symmetric contribution of the voltage which has major contributions from spin-pumping and anisotropic magnetoresistance (AMR).  $V_A$  is the anti-symmetric part, which consists of effects from AMR, anomalous Hall and planar Hall effects (AHE, PHE)(47).

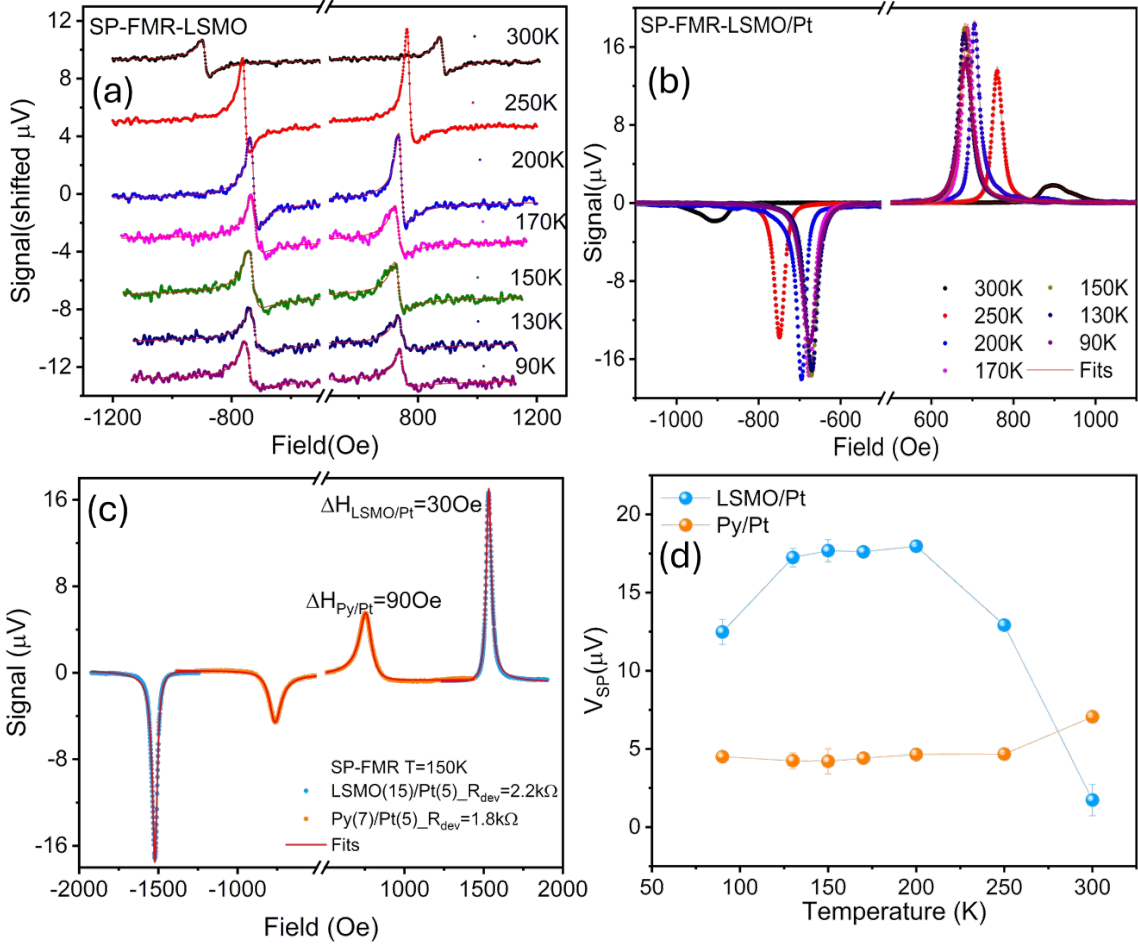


Figure 6 SP-FMR results (a)-(b) show the obtained spectra at 5 GHz for LSMO and LSMO/Pt respectively. The signal for LSMO has been shifted for clarity. For LSMO/Pt, the signal increases with lower temperatures and is dominated by spin pumping contribution. The red solid lines indicate fits to Eq 4. (c) shows comparative SP-FMR signal strength between Py(7)/Pt(5) and LSMO(15)/Pt(5) on NGO(110) substrate at 150K and 8 GHz (d) shows the comparison of the SP-FMR voltage for LSMO/Pt and Py/Pt at 8GHz for different temperatures.

We first perform SP-FMR measurements at 31.6 mW RF power at different temperatures on patterned LSMO films (Fig. 6(a)) to rule out any contribution to the spin pumping signal arising from single layer LSMO. First, we focus on signal strength. The overall peak-to-peak voltage amplitude is less at 300K (<1uV) and attains a maximum around 200K (3uV), which can be attributed to the increase in  $M_s$  and a stronger exchange interaction strength at lower temperature. Below 170 K, the signal strength decreases. This behavior suggests a larger dissipation of the angular momentum below 170 K. This can be within the bulk of the film and/or due to increased interaction with the PSMA layers. We can see that at all temperatures, the signal has the same shape in the positive and the negative field directions, indicating negligible spin-pumping contribution. This signal mainly arises from AMR effect, which has symmetric and antisymmetric contributions, and the AHE effect which has a dominant anti-symmetric contribution in this measurement configuration(10, 47). As we go down in temperature, the anti-symmetric contribution reduces, indicating a reduction in the AHE effects. This can be due to the combined effect of reduction of resistivity of LSMO(48) with decreasing temperature and increased absorption of the angular momentum within the bulk/PSMA layers. These measurements confirm the increased dissipation of spin

angular momentum at lower temperatures, and that LSMO by itself does not convert the scattered spins into a measurable spin-pumping voltage.

Figure 6(b) shows the SP-FMR signal of LSMO/Pt. A stark contrast is observed in the line-shape and signal strength. The signal sign exhibits an odd symmetry with respect to positive and negative field directions and has a dominant symmetric component. The symmetric component is 5-10 times greater in signal strength with respect to LSMO. This indicates that LSMO/Pt total voltage has a significant contribution from spin pumping(47, 49). Moreover, the observed behavior is primarily governed by the properties at the LSMO/Pt interface.

For 300K, the LSMO/Pt signal is quite broad and is composed of two modes, similar to that observed in the FMR spectrum. This may be due to multiple non-uniform modes due to a lower exchange interaction energy and/or magnetic inhomogeneities present in LSMO(18). However, as the temperature decreases, the signal values increase drastically from 2 $\mu$ V at 300K to 18 $\mu$ V at 200K with presence of a sharper single mode. This behavior is similar to the FMR spectrum, which can be attributed to a stronger FM exchange coupling in LSMO at lower temperature, enabling uniform collective oscillation, and consequently a higher magnitude of spin pumping into Pt. The signal attains a maximum value between 200-170K, which then reduces to 12  $\mu$ V at 90K. The linewidths from SP-FMR and FMR show a similar trend to the damping. The SP-FMR (FMR) linewidth reduces drastically from 64 Oe (62Oe) at 300K to a minimum of 24 Oe (11Oe) at 200K and then increases to 38 Oe (25Oe) at 90K. The increased linewidth of LSMO/Pt in the SP-FMR measurements with respect to FMR spectra may be due to some sample differences during device fabrication. The linewidth variation of single layer LSMO devices shows more randomness as opposed to LSMO/Pt devices (Fig. S6(c)). This indicates that deposition of the Pt layer (in spite of being *ex situ*) protects the device from extensive sample damage, which is advantageous for device fabrication. Further, upon comparing the relative signal strength and device resistance of LSMO(15)/Pt(5) with that of Py(7)/Pt(5), we clearly see the advantages of LSMO/Pt system (Fig. 6(c)-(d)). The signal strength at 150K is 4 times higher in LSMO/Pt (17.8 $\mu$ V) as opposed to Py/Pt (4  $\mu$ V) for comparable device resistances. It is also to be noted that the damping and linewidths for Py(7) and Pt(7)/Py(5) system are consistently higher than LSMO and LSMO/Pt respectively and remain almost constant with temperature (Fig. 3(c) and Fig. S7(a) respectively).

The spin Hall angle ( $\theta_{SHA}$ ) is the figure of merit to determine the charge to spin conversion ratio. We obtain  $\theta_{SHA}$  through the following equation(10, 50):

$$I_{SP} = \theta_{SHA} J_s w \lambda_{sf} \tanh\left(\frac{t_{Pt}}{2 \lambda_{sf}}\right). \quad (5)$$

Here  $I_{SP}$  is the spin-pumping current obtained by  $(V_{S+} - V_{S-}) / (2R_{dev})$ .  $V_{S+(-)}$  is the spin pumping voltage at positive (negative) fields.  $R_{dev}$  is the resistance of the device,  $t_{Pt}$  is the thickness of Pt (5 nm),  $w$  is the width of the device (10  $\mu$ m) and  $\lambda_{sf}$  is the spin diffusion length of Pt, which we have assumed to be 3.4 nm(7).  $J_s$  is the spin current density is determined by the following relation(10, 50) :

$$J_s \approx \left( \frac{g_{eff}^{\uparrow\downarrow} \hbar}{8\pi} \right) \left( \frac{h_{rf} \gamma}{\alpha} \right)^2 \left[ \frac{4\pi M_{eff} \gamma + \sqrt{(4\pi M_{eff} \gamma)^2 + (4\pi f)^2}}{(4\pi M_{eff} \gamma)^2 + (4\pi f)^2} \right] \left( \frac{2e}{\hbar} \right). \quad (6)$$

Here  $e$  is the electronic charge and  $h_{RF}$  is the RF field experienced by the sample which was calibrated beforehand for all RF frequencies(46) and  $g_{eff}$  is the effective spin mixing conductance given as

$$g_{eff}^{\uparrow\downarrow} = \frac{4\pi M_s d_{FM} \Delta\alpha}{g\mu_B} \quad (51),$$

where  $g$  is the g-factor obtained from the Kittel fittings of sample LSMO/Pt (Fig. S5(c)),  $\mu_B$  is the Bohr magneton.  $\Delta\alpha$  is the difference between the damping of samples LSMO/Pt and LSMO ( $\alpha_{LSMO/Pt} - \alpha_{LSMO}$ ) obtained by FMR,  $d_{FM}$  is the thickness of the ferromagnetic layer (15 nm).

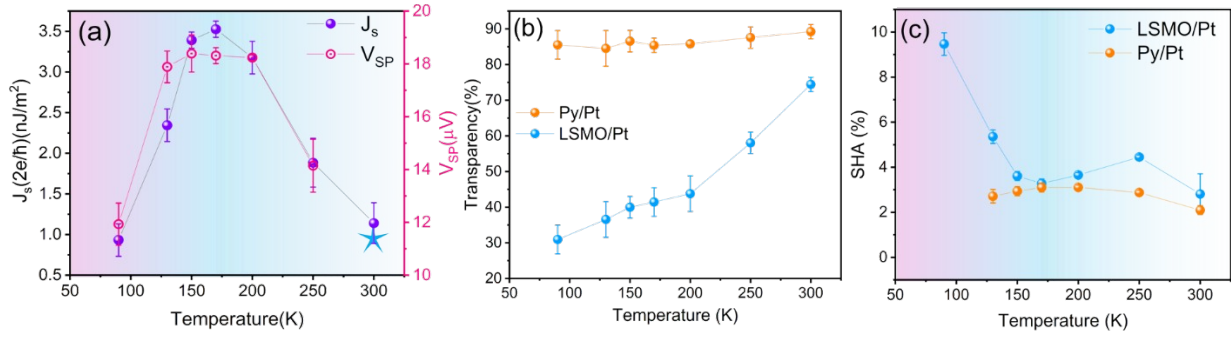


Figure 7 SHA determination from SP-FMR results. (a) shows the variation of the spin current density into the Pt layer with temperature for LSMO/Pt along with the spin pumping voltages at different temperatures at 5GHz. VSP for 300K is not plotted as the two-mode fitting may not provide a reliable value unlike single mode fitting for lower temperatures. The star indicates a value of 0.75 n/m<sup>2</sup> for LSMO/Pt system as reported in literature (20). (b) Shows the variation of the interfacial transparency for LSMO/Pt. (c) shows the variation of the spin Hall angle with respect to temperature.

The variation of  $J_s$  vs. temperature for LSMO/Pt is shown in Fig. 7(a). We see that the spin current increases with decreasing temperature down to 170K, which can be attributed to the increased magnetization of the LSMO, resulting in greater spin pumping into the system. Below 150K, the  $J_s$  decreases, which may be attributed to absorption of some of the spin current being pumped into Pt, due to enhanced interaction between the metallic LSMO and the PSMA layer at LSMO/Pt interface, which is also reflected in the variation of the  $V_{SP}$ .

To further shed light on this behavior of  $J_s$ , we track the behavior of the spin transparency ( $T$ ) at the LSMO/Pt interface which is given as (11, 52):

$$T = \frac{g_r \tanh\left(\frac{t_{Pt}}{\lambda_{Pt}}\right)}{g_r \coth\left(\frac{t_{Pt}}{\lambda_{Pt}}\right) + \frac{h}{2e^2 \rho_{Pt} \lambda_{Pt}}} \quad (7)$$

Here  $g_r$  is the real part of  $g_{eff}$  and we have assumed  $g_r = g_{eff}$  (11). The interfacial transparency decreases with temperature from 76% at RT to 30% at 90K at the LSMO/Pt (Fig. 7(b)). The different Mn valence layer at the top interface likely exhibit a different electronic variation with temperature than the bulk, resulting in poorer electronic structure matching with the overlying Pt, consequently lowering spin transparency. The reduction of the spin transparency  $T$  can be interpreted as a direct consequence of the PSMA layer scattering the spin currents going into Pt. However, the simultaneous increase of the  $M_s$  and FM exchange interaction strength leads to stronger moment precession of LSMO, thus dominating the reduction in the spin transparency. However, the  $M_s$  saturates below  $T < 150$ K and the scattering of the spin current at the top PSMA layer becomes dominant, due to the increased interaction between the different Mn valence states, leading to a decrease in the  $J_s$ . This is in stark contrast to the in-situ deposited Py/Pt system, where the spin transparency remains almost constant throughout the temperature range. Further explicit analysis of the temperature dependent variation of electronic and magnetic nature of the bulk and interfacial layers would require detailed X-ray absorption spectroscopy, which is beyond the scope of this work.

Figure 7(c) shows the variation of the spin Hall angle with respect to temperature. At 300 K, we obtain a  $\theta_{SHA}$  of  $\approx 2.3\%$ . It then increases and varies from 4.4 to 3 % from 250K-150K. The  $\theta_{SHA}$  then increases to  $\approx 9\%$  at 90K. The large error margin of SHA at 300 K is due to low spin pumping signal, the strength of which is split between two modes. At lower temperatures, only one mode emerges with a strong spin pumping voltage, resulting in a more consistent value of the  $\theta_{SHA}$  (down to  $T=150$  K). However, upon further decreasing the temperature (130-90 K), the interaction between the bulk of LSMO with the PSMA region increases, which further enhances the damping. From Eq. 6, we can see that the  $\theta_{SHA}$  is directly proportional to the overall damping of the system. Thus, this additional increase in damping leads to a seemingly increased value of  $\theta_{SHA}$  which may not reflect the true spin-charge conversion efficiency. In the temperature regime where this interaction is inconsequential ( $250\text{K} < T < 170\text{K}$ ), the obtained value of the spin Hall angle between is consistent with the measured Py/Pt sample and also with many reports involving Pt/FM systems(7, 11, 16, 45, 53).

Despite the *ex-situ* nature of fabrication, we found that the LSMO/Pt exhibit robust SP-FMR signals at all temperatures ranging from 300K to 90K. We report the lowest observed damping for LSMO(15)/Pt(5) system at 170K ( $0.0020 \pm 0.0005$ ), almost 2-3 times lower than values reported to date(16–18, 20), for systems with comparable or larger LSMO thicknesses. Further the thin film properties show an 8-fold reduction in damping for LSMO/Pt as opposed to Py/Pt (Fig. 3(c)). The thin LSMO and Pt layers allow for pronounced interfacial effects in the system, leading to generation of strong spin pumping voltage signals in micron size devices. Further, we report a sharp FMR linewidth at ( $12 \pm 1$  Oe at 170K and 5 GHz) with a robust spin Hall angle ( $3.2 \pm 0.4\%$ ). EELS measurements revealed PSMA layers at the top and bottom LSMO interfaces which have a reduced Mn valence state as opposed to the bulk. While the PSMA layer may contribute to an increase in damping due to increased magnetic interaction with the bulk LSMO moments, it does not contribute to spin pumping through the entire temperature range. The spin current pumped into Pt is the maximum at 170 K ( $3.5 \pm 0.1$  nJ/m<sup>2</sup>) which then decreases with reducing temperature due to spin scattering effect arising from the increased interaction between spins of metallic LSMO with that of top PSMA layers of LSMO. This is corroborated by the interfacial transparency calculations and comparison with Py/Pt system. While the PSMA layer hinders spin current transmission at low temperatures, this issue can potentially be mitigated through several approaches. These include in-

situ deposition to ensure a cleaner interface, the use of epitaxial oxide heterostructure capping and buffer layers such as  $\text{SrTiO}_3$  to reduce octahedra rotation and formation of dead layers (41), and heterointerface engineering via the deposition of thin layers like  $\text{La}_{0.33}\text{Sr}_{0.67}\text{O}$  to allow for cleaner growth of LSMO (54), among others. Comparison of device performance of LSMO/Pt with popularly used Py/Pt for  $150\text{K} < T < 200\text{K}$  shows a 4 times larger signal output with 3 times lower linewidth for similar device resistances and 8 times lower Gilbert damping at 170K. All these properties point to the robustness of using this bilayer system as an energy-efficient spintronic device for applications such as low-power nano-oscillators.

### **Acknowledgements:**

This work was primarily supported as part of Quantum Materials for Energy Efficient Neuromorphic Computing (Q-MEEN-C), an Energy Frontier Research Center funded by the U.S. Department of Energy (DOE), Office of Science, Basic Energy Sciences (BES), under Award # DE-SC0019273.

This material is based upon research partially supported by the Chateaubriand Fellowship of the Office for Science & Technology of the Embassy of France in the United States.

Devices were patterned at Jean Lamour Institute's cleanroom platform, MiNaLor, which is partially funded by the Grand Est region via the project RANGE. We also acknowledge the support from EU-H2020-RISE project Ultra Thin Magneto Thermal Sensing ULTIMATE-I (Grant ID. 101007825).

This work was partially supported by the project "Lorraine Université d'Excellence" reference ANR-15-IDEX-04-LUE, through the France 2030 government grants EMCOM (ANR-22-PEEL-0009), and PEPR SPIN – SPINMAT ANR-22-EXSP-0007.

### **References:**

1. M. Tarequzzaman, T. Böhnert, M. Decker, J. D. Costa, J. Borme, B. Lacoste, E. Paz, A. S. Jenkins, S. Serrano-Guisan, C. H. Back, R. Ferreira, P. P. Freitas, Spin torque nano-oscillator driven by combined spin injection from tunneling and spin Hall current. *Commun. Phys.* **2**, 1–8 (2019).
2. H. S. Choi, S. Y. Kang, S. J. Cho, I.-Y. Oh, M. Shin, H. Park, C. Jang, B.-C. Min, S.-I. Kim, S.-Y. Park, C. S. Park, Spin nano-oscillator-based wireless communication. *Sci. Rep.* **4**, 5486 (2014).
3. J. Grollier, D. Querlioz, K. Y. Camsari, K. Everschor-Sitte, S. Fukami, M. D. Stiles, Neuromorphic spintronics. *Nat. Electron.* **3**, 360–370 (2020).
4. M. Carpentieri, G. Finocchio, “Chapter 7 - Spintronic Oscillators Based on Spin-Transfer Torque and Spin-Orbit Torque” in *Handbook of Surface Science*, R. E. Camley, Z. Celinski, R. L. Stamps, Eds. (North-Holland, 2015); <https://www.sciencedirect.com/science/article/pii/B9780444626349000072>)vol. 5 of *Magnetism of Surfaces, Interfaces, and Nanoscale Materials*, pp. 297–334.
5. V. E. Demidov, S. Urazhdin, A. Zholud, A. V. Sadovnikov, S. O. Demokritov, Nanoconstriction-based spin-Hall nano-oscillator. *Appl. Phys. Lett.* **105**, 172410 (2014).
6. M. Zahedinejad, H. Mazraati, H. Fulara, J. Yue, S. Jiang, A. A. Awad, J. Åkerman, CMOS compatible W/CoFeB/MgO spin Hall nano-oscillators with wide frequency tunability. *Appl. Phys. Lett.* **112**, 132404 (2018).
7. J.-C. Rojas-Sánchez, N. Reyren, P. Laczkowski, W. Savero, J.-P. Attané, C. Deranlot, M. Jamet, J.-M. George, L. Vila, H. Jaffrès, Spin Pumping and Inverse Spin Hall Effect in Platinum: The Essential Role of Spin-Memory Loss at Metallic Interfaces. *Phys. Rev. Lett.* **112**, 106602 (2014).
8. K. Ando, S. Takahashi, J. Ieda, Y. Kajiwara, H. Nakayama, T. Yoshino, K. Harii, Y. Fujikawa, M. Matsuo, S. Maekawa, E. Saitoh, Inverse spin-Hall effect induced by spin pumping in metallic system. *J. Appl. Phys.* **109**, 103913 (2011).
9. S.-I. Kim, D.-J. Kim, M.-S. Seo, B.-G. Park, S.-Y. Park, Dependence of inverse-spin Hall effect and spin-rectified voltage on tantalum thickness in Ta/CoFeB bilayer structure. *Appl. Phys. Lett.* **106**, 032409 (2015).
10. B. Sahoo, K. Roy, P. Gupta, A. Mishra, B. Satpati, B. B. Singh, S. Bedanta, Spin Pumping and Inverse Spin Hall Effect in Iridium Oxide. *Adv. Quantum Technol.* **4**, 2000146 (2021).
11. B. Sahoo, A. Frano, Eric. E. Fullerton, Efficient charge to spin conversion in iridium oxide thin films. *Appl. Phys. Lett.* **123**, 032404 (2023).
12. C.-F. Pai, L. Liu, Y. Li, H. W. Tseng, D. C. Ralph, R. A. Buhrman, Spin transfer torque devices utilizing the giant spin Hall effect of tungsten. *Appl. Phys. Lett.* **101**, 122404 (2012).

13. Q. Qin, S. He, W. Song, P. Yang, Q. Wu, Y. P. Feng, J. Chen, Ultra-low magnetic damping of perovskite  $\text{La}_{0.7}\text{Sr}_{0.3}\text{MnO}_3$  thin films. *Appl. Phys. Lett.* **110**, 112401 (2017).
14. J.-H. Park, E. Vescovo, H.-J. Kim, C. Kwon, R. Ramesh, T. Venkatesan, Direct evidence for a half-metallic ferromagnet. *Nature* **392**, 794–796 (1998).
15. I. N. Krivorotov, K. R. Nikolaev, A. Yu. Dobin, A. M. Goldman, E. D. Dahlberg, Exchange Field Induced Magnetoresistance in Colossal Magnetoresistance Manganites. *Phys. Rev. Lett.* **86**, 5779–5782 (2001).
16. P. Gupta, B. B. Singh, K. Roy, A. Sarkar, M. Waschk, T. Brueckel, S. Bedanta, Simultaneous observation of anti-damping and the inverse spin Hall effect in the  $\text{La}_{0.7}\text{Sr}_{0.3}\text{MnO}_3/\text{Pt}$  bilayer system. *Nanoscale* **13**, 2714–2719 (2021).
17. V. A. Atsarkin, B. V. Sorokin, I. V. Borisenko, V. V. Demidov, G. A. Ovsyannikov, Resonance spin-charge phenomena and mechanism of magnetoresistance anisotropy in manganite/metal bilayer structures. *J. Phys. Appl. Phys.* **49**, 125003 (2016).
18. H. K. Lee, I. Barsukov, A. G. Swartz, B. Kim, L. Yang, H. Y. Hwang, I. N. Krivorotov, Magnetic anisotropy, damping, and interfacial spin transport in Pt/LSMO bilayers. *AIP Adv.* **6**, 055212 (2016).
19. G. Y. Luo, J. G. Lin, W.-C. Chiang, C.-R. Chang, Spin pump and probe in lanthanum strontium manganite/platinum bilayers. *Sci. Rep.* **7**, 6612 (2017).
20. I. Benguettat-EL Mokhtari, Y. Roussigné, T. Petrisor Jr., F. Zighem, F. Kail, L. Chahed, V. Pierron, L. Méchin, M. Gabor, M. Belmeguenai, Spin Pumping and Magnetic Anisotropy in  $\text{La}_{2/3}\text{Sr}_{1/3}\text{MnO}_3/\text{Pt}$  Systems. *Phys. Status Solidi B* **257**, 2000265 (2020).
21. V. A. Atsarkin, I. V. Borisenko, V. V. Demidov, T. A. Shaikhulov, Temperature dependence of pure spin current and spin-mixing conductance in the ferromagnetic—normal metal structure. *J. Phys. Appl. Phys.* **51**, 245002 (2018).
22. L. Liu, T. Moriyama, D. C. Ralph, R. A. Buhrman, Spin-Torque Ferromagnetic Resonance Induced by the Spin Hall Effect. *Phys. Rev. Lett.* **106**, 036601 (2011).
23. M. S. Alias, Y. Yang, T. K. Ng, I. Dursun, D. Shi, M. I. Saidaminov, D. Priante, O. M. Bakr, B. S. Ooi, Enhanced Etching, Surface Damage Recovery, and Submicron Patterning of Hybrid Perovskites using a Chemically Gas-Assisted Focused-Ion Beam for Subwavelength Grating Photonic Applications. *J. Phys. Chem. Lett.* **7**, 137–142 (2016).
24. R. Trappen, A. J. Grutter, C.-Y. Huang, A. Penn, N. Mottaghi, S. Yousefi, A. Haertter, S. Kumari, J. LeBeau, B. J. Kirby, M. B. Holcomb, Effect of oxygen stoichiometry on the magnetization profiles and negative magnetization in LSMO thin films. *J. Appl. Phys.* **126**, 105301 (2019).

25. V. Haspot, P. Noël, J.-P. Attané, L. Vila, M. Bibes, A. Anane, A. Barthélémy, Temperature dependence of the Gilbert damping of  $\text{La}_{0.7}\text{Sr}_{0.3}\text{MnO}_3$  thin films. *Phys. Rev. Mater.* **6**, 024406 (2022).
26. Y. Wang, X. Fan, X. Feng, X. Gao, Y. Ke, J. Yao, M. Guo, T. Wang, L. Shen, M. Liu, D. Xue, X. Fan, Thickness and temperature-dependent damping in  $\text{La}_{0.67}\text{Sr}_{0.33}\text{MnO}_3$  epitaxial films. *Appl. Phys. Lett.* **123**, 112403 (2023).
27. D. Jiang, H. Chen, G. Ji, Y. Chai, C. Zhang, Y. Liang, J. Liu, W. Skowroński, P. Yu, D. Yi, T. Nan, Substrate-induced spin-torque-like signal in spin-torque ferromagnetic resonance measurement. *Phys. Rev. Appl.* **21**, 024021 (2024).
28. L. Méchin, S. Wu, B. Guillet, P. Perna, C. Fur, S. Lebargy, C. Adamo, D. G. Schlom, J. M. Routoure, Experimental evidence of correlation between  $1/f$  noise level and metal-to-insulator transition temperature in epitaxial  $\text{La}_{0.7}\text{Sr}_{0.3}\text{MnO}_3$  thin films. *J. Phys. Appl. Phys.* **46**, 202001 (2013).
29. S. Dutta, K. Sankaran, K. Moors, G. Pourtois, S. Van Elshocht, J. Bömmels, W. Vandervorst, Z. Tókei, C. Adelman, Thickness dependence of the resistivity of platinum-group metal thin films. *J. Appl. Phys.* **122**, 025107 (2017).
30. V. V. Demidov, G. A. Ovsyannikov, Temperature dependence of interlayer exchange interaction in  $\text{La}_{0.7}\text{Sr}_{0.3}\text{MnO}_3/\text{SrRuO}_3$  heterostructure. *J. Appl. Phys.* **122**, 013902 (2017).
31. C. Kittel, On the Theory of Ferromagnetic Resonance Absorption. *Phys. Rev.* **73**, 155–161 (1948).
32. H. B. Vasili, M. Gamino, J. Gàzquez, F. Sánchez, M. Valvidares, P. Gargiani, E. Pellegrin, J. Fontcuberta, Magnetoresistance in Hybrid Pt/CoFe<sub>2</sub>O<sub>4</sub> Bilayers Controlled by Competing Spin Accumulation and Interfacial Chemical Reconstruction. *ACS Appl. Mater. Interfaces* **10**, 12031–12041 (2018).
33. J. Fontcuberta, H. B. Vasili, J. Gàzquez, F. Casanova, On the Role of Interfaces on Spin Transport in Magnetic Insulator/Normal Metal Heterostructures. *Adv. Mater. Interfaces* **6**, 1900475 (2019).
34. L. J. Zhu, D. C. Ralph, R. A. Buhrman, Irrelevance of magnetic proximity effect to spin-orbit torques in heavy-metal/ferromagnet bilayers. *Phys. Rev. B* **98**, 134406 (2018).
35. R. Arias, D. L. Mills, Extrinsic contributions to the ferromagnetic resonance response of ultrathin films. *Phys. Rev. B* **60**, 7395–7409 (1999).
36. I. Barsukov, P. Landeros, R. Meckenstock, J. Lindner, D. Spoddig, Z.-A. Li, B. Krumme, H. Wende, D. L. Mills, M. Farle, Tuning magnetic relaxation by oblique deposition. *Phys. Rev. B* **85**, 014420 (2012).
37. V. Kamberský, On ferromagnetic resonance damping in metals. *Czechoslov. J. Phys. B* **26**, 1366–1383 (1976).

38. B. Heinrich, D. Fraitová, V. Kamberský, The Influence of s-d Exchange on Relaxation of Magnons in Metals. *Phys. Status Solidi B* **23**, 501–507 (1967).
39. V. Korenman, R. E. Prange, Anomalous Damping of Spin Waves in Magnetic Metals. *Phys. Rev. B* **6**, 2769–2777 (1972).
40. Z. Liao, N. Gauquelin, R. J. Green, S. Macke, J. Gonnissen, S. Thomas, Z. Zhong, L. Li, L. Si, S. Van Aert, P. Hansmann, K. Held, J. Xia, J. Verbeeck, G. Van Tendeloo, G. A. Sawatzky, G. Koster, M. Huijben, G. Rijnders, Thickness Dependent Properties in Oxide Heterostructures Driven by Structurally Induced Metal–Oxygen Hybridization Variations. *Adv. Funct. Mater.* **27**, 1606717 (2017).
41. Z. Li, M. Bosman, Z. Yang, P. Ren, L. Wang, L. Cao, X. Yu, C. Ke, M. B. H. Breese, A. Rusydi, W. Zhu, Z. Dong, Y. L. Foo, Interface and Surface Cation Stoichiometry Modified by Oxygen Vacancies in Epitaxial Manganite Films. *Adv. Funct. Mater.* **22**, 4312–4321 (2012).
42. Y. Wei, R. Brucas, K. Gunnarsson, Z. Celinski, P. Svedlindh, Positive correlation between coercivity and ferromagnetic resonance extrinsic linewidth in FeCoV/SiO<sub>2</sub> films. *Appl. Phys. Lett.* **104**, 072404 (2014).
43. S. Zhang, P. M. Levy, Enhanced Spin-Dependent Scattering at Interfaces. *Phys. Rev. Lett.* **77**, 916–919 (1996).
44. C. Zener, Interaction between the d -Shells in the Transition Metals. II. Ferromagnetic Compounds of Manganese with Perovskite Structure. *Phys. Rev.* **82**, 403–405 (1951).
45. T. Fache, J. C. Rojas-Sanchez, L. Badie, S. Mangin, S. Petit-Watelot, Determination of spin Hall angle, spin mixing conductance, and spin diffusion length in CoFeB/Ir for spin-orbitronic devices. *Phys. Rev. B* **102**, 064425 (2020).
46. I. C. Arango, A. Anadón, S. Novoa, V. T. Pham, W. Y. Choi, J. Alegre, L. Badie, A. Chuvilin, S. Petit-Watelot, L. E. Hueso, F. Casanova, J.-C. Rojas-Sánchez, Spin-to-charge conversion by spin pumping in sputtered polycrystalline Bi<sub>x</sub>Se<sub>1-x</sub>. *Phys. Rev. Mater.* **7**, 075402 (2023).
47. M. Harder, Y. Gui, C.-M. Hu, Electrical detection of magnetization dynamics via spin rectification effects. *Phys. Rep.* **661**, 1–59 (2016).
48. N. Nagaosa, J. Sinova, S. Onoda, A. H. MacDonald, N. P. Ong, Anomalous Hall effect. *Rev. Mod. Phys.* **82**, 1539–1592 (2010).
49. A. Conca, B. Heinz, M. R. Schweizer, S. Keller, E. Th. Papaioannou, B. Hillebrands, Lack of correlation between the spin-mixing conductance and the inverse spin Hall effect generated voltages in CoFeB/Pt and CoFeB/Ta bilayers. *Phys. Rev. B* **95**, 174426 (2017).
50. K. Rogdakis, A. Sud, M. Amado, C. M. Lee, L. McKenzie-Sell, K. R. Jeon, M. Cubukcu, M. G. Blamire, J. W. A. Robinson, L. F. Cohen, H. Kurebayashi, Spin

transport parameters of NbN thin films characterized by spin pumping experiments. *Phys. Rev. Mater.* **3**, 014406 (2019).

51. Y. Tserkovnyak, A. Brataas, G. E. W. Bauer, Spin pumping and magnetization dynamics in metallic multilayers. *Phys. Rev. B* **66**, 224403 (2002).
52. W. Zhang, W. Han, X. Jiang, S.-H. Yang, S. S. P. Parkin, Role of transparency of platinum-ferromagnet interfaces in determining the intrinsic magnitude of the spin Hall effect. *Nat. Phys.* **11**, 496–502 (2015).
53. X. Tao, Q. Liu, B. Miao, R. Yu, Z. Feng, L. Sun, B. You, J. Du, K. Chen, S. Zhang, L. Zhang, Z. Yuan, D. Wu, H. Ding, Self-consistent determination of spin Hall angle and spin diffusion length in Pt and Pd: The role of the interface spin loss. *Sci. Adv.* **4**, eaat1670 (2018).
54. H. Boschker, J. Verbeeck, R. Egoavil, S. Bals, G. van Tendeloo, M. Huijben, E. P. Houwman, G. Koster, D. H. A. Blank, G. Rijnders, Preventing the Reconstruction of the Polar Discontinuity at Oxide Heterointerfaces. *Adv. Funct. Mater.* **22**, 2235–2240 (2012).